Sea surface height anomalies of the Arctic Ocean from ICESat-2: a first examination and comparisons with CryoSat-2

M. Bagnardi[1,2], N. Kurtz[1], A. A. Petty[1,3], R. Kwok[4]

[1]Cryospheric Sciences Laboratory, NASA Goddard Space Flight Center, Beltsville, MD, United States.

[2]ADNET Systems, Inc., Bethesda, MD, United States.

[3]Earth System Interdisciplinary Center, University of Maryland, College Park, MD, United States.

[4]Polar Science Center, Applied Physics Laboratory, University of Washington, Seattle, WA, United States.

Corresponding author: Marco Bagnardi (marco.bagnardi@nasa.gov)

Key Points:

- We present the first (multi-year) examination of Arctic Ocean sea surface height anomalies (SSHA) from the ICESat-2 laser altimeter.
- ICESat-2 SSHA estimates compare well with near-coincident (*CRYO2ICE*) radar altimetry-derived SSHA estimates from CryoSat-2.
- ICESat-2 and CryoSat-2 show good agreement in the seasonal variability in SSHA suggesting ICESat-2 adds to the time-series of Arctic SSHA.

Abstract.

Accurately resolving spatio-temporal variations in sea surface height across the polar oceans is key to improving our understanding of ocean circulation variability and change. Here, we examine the first two years (2018-2020) of Arctic Ocean sea surface height anomalies (SSHA) from the photon-counting laser altimeter onboard NASA's ICE, Cloud, and Land Elevation Satellite-2 (ICESat-2). ICESat-2 SSHA estimates are compared to estimates from ESA's CryoSat-2 mission, including semi-synchronous along-track measurements from the recent *CRYO2ICE* orbit alignment campaign. There are documented residual centimeter-scale range biases between the ICESat-2 beams (in release-003 data) and we opted for a single-beam approach in our comparisons. We find good agreement in the along-track estimates (spatial correlation coefficient >0.8 and mean differences <0.03 m) as well as in the gridded monthly SSHA estimates (temporal correlation coefficient of 0.76 and a mean difference of 0.01 m) from the two altimeters, suggesting ICESat-2 adds to the CryoSat-2 SSHA estimates.

Plain Language Summary

The polar oceans, with warming and dramatic declines in sea ice coverage, are experiencing some of the most rapid environmental changes on Earth. These changes have direct impacts on ocean circulation and freshwater distribution, with observable changes in sea surface height. Measuring and monitoring basin-scale variability of sea level of the ice-covered oceans has proven challenging because the surface of these oceans is only exposed within narrow openings in the sea ice, requiring high spatial resolution and bespoke measurement techniques. This study takes a first look at new high-resolution laser altimetry measurements of sea level over the Arctic Ocean collected by NASA's ICESat-2 satellite since its launch in 2018. We compare the results with those obtained using independent data from ESA's CryoSat-2 satellite radar altimeter. By looking at near-synchronous data from when the orbits of the two satellites coincide over the Arctic Ocean, and by comparing sea surface height maps from both sensors during the two years of overlap (2018-2020) between the two missions, we find good agreement between the sea surface height estimates, providing additional confidence that ICESat-2 can be used to infer regional and seasonal polar sea surface height variability.

1 Introduction

Satellite observations of the Arctic Ocean have shown significant changes in ocean circulation, fresh water storage and energy balance since at least the 1980s, (Armitage et al., 2020; Morison et al., 2012, 2021; Polyakov et al., 2017; Proshutinsky et al., 2019; Timmermans & Marshall, 2020). Routine and accurate profiling of the sea surface height (SSH) in the Arctic is needed to continue these crucial time-series and provide more detailed insights into these changes. While we can reliably monitor the SSH of the open oceans at low-to-mid latitudes using satellite altimetry data (IPCC, 2019), continuous and widespread measurements at high-latitude ice-covered seas have remained limited. The main challenges are the reduced coverage due to the low inclination orbit of most satellite altimeters, sea surface sampling limited to narrow openings in the sea ice cover, and the need to accurately discriminate between sea ice and ocean surface altimetry returns.

Measurements of Arctic SSH from satellite altimetry started with low resolution radar data collected by the European Space Agency's (ESA) ERS and Envisat radar missions (1995–2010; Giles et al., 2012; Peacock & Laxon, 2004). However, the orbit inclination of these satellites limited measurements to 81.5° latitude. NASA's ICESat satellite, which operated between 2003 and 2009 (Zwally et al., 2002), offered higher resolution lidar data that improved lead classification and SSH estimates (Kwok & Morison, 2011) while its orbit inclination resulted in more extensive coverage of the Arctic Ocean. Since 2010, ESA's CryoSat-2 satellite has been acquiring unfocussed synthetic aperture radar (SAR) altimetry data over the polar regions (Parrinello et al., 2018; Wingham et al., 2006). CryoSat-2's high orbit inclination and continuous data collection have enabled basin-scale mapping of seasonal and interannual SSH variability up to 88° latitude. The SSH data from CryoSat-2 have been compared with Arctic tide gauge measurements and ocean mass variations (e.g., GRACE) and basin-scale, monthly, estimates of dynamic ocean topography (DOT; Armitage et al., 2016, 2018; Kwok & Morison, 2016) have been produced.

In September 2018, NASA launched the Ice, Cloud, and Land Elevation Satellite-2 (ICESat-2) laser altimetry mission, which has since been providing year-round profiling of the Earth's surface up to 88° latitude (Neumann et al., 2019). The novel photon-counting Advanced Topographic Laser Altimeter (ATLAS) on ICESat-2 provides high-resolution surface height measurements across its six-beam configuration. For the polar oceans, the data collected by ICESat-2 are currently being used to produce routine estimates of sea ice height, type (e.g., lead/ice), and freeboard (Kwok et al., 2021a). The ICESat-2 processing algorithms utilize specular returns to discriminate open-water leads from sea ice, and the laser's spatial resolution (~11 m diameter footprint; Magruder et al., 2020) is significantly higher than that of CryoSat-2 (380 m along-track and 1650 m across-track pulse limited footprint; Scagliola, 2013). Also, contamination by off-nadir specular returns from up to 15 km across-track can potentially bias CryoSat-2 surface height retrievals (Armitage & Davidson, 2014). New waveform processing techniques have been developed, which could help account for these off-nadir returns and improve lead height retrievals (e.g., Di Bella et al., 2020). On the other hand, laser altimetry measurements are often hindered by the presence of clouds, which are otherwise penetrated by radar. Measurements of sea ice height and freeboard by ICESat-2 have been validated against coincident laser profiles collected during targeted underflights by NASA’s Operation IceBridge (OIB) airborne mission (Kwok et al., 2019) and the sea ice classification algorithm has been shown to agree well with coincident imagery (Kwok et al., 2021b; Petty et al., 2021). At the time of writing, ICESat-2 SSH measurements have yet to be compared against independent height data (e.g., tide gauges, measurements from other airborne or satellite missions).

As of August 2020, the orbit of CryoSat-2 has been modified as part of the *CRYO2ICE* campaign (https://earth.esa.int/eogateway/missions/cryosat/cryo2ice), such that every 19 orbits (20 orbits for ICESat-2) the two satellites are aligned for hundreds of kilometers over the Arctic Ocean, acquiring data along near-coincident ground tracks with a minimum time difference of approximately three hours (https://cryo2ice.org/). In this study, we present a first comparison of semi-synchronous along-track SSHA retrievals from ICESat-2 and CryoSat-2 from four *CRYO2ICE* profiles. We examine SSHA from individual ICESat-2 beams and assess inter-beam range biases. We produce gridded SSHA composite maps of the Arctic Ocean and examine the relative agreement of the monthly, seasonal, and multi-year SSHA from the two altimeters. Daily/monthly gridded SSHA measurements over both polar oceans are planned to be released as an official ICESat-2 data product (ATL21) in Summer 2021, and this study offers an examination of this type of composite SSHA data over the Arctic.

2 Data and Methods

2.1 ICESat-2 data

The ICESat-2 photon-counting laser altimeter transmits laser pulses split into a six-beam configuration of three beam pairs (each having a strong and a weak beam), where beam numbers 1, 3, and 5 identify the strong beams, and 2, 4, and 6 the weak beams (Neumann et al., 2019). The 10 kHz pulse repetition rate leads to a 0.7 m along-track separation between subsequent laser pulses of the ~11 m lidar footprint (Magruder et al., 2020). Among the ICESat-2 data products, the Level 3A sea ice products ATL07 (sea ice height and type, https://nsidc.org/data/ATL07) and ATL10 (freeboard, https://nsidc.org/data/ATL10) provide along-track measurements for six individual ground tracks (targeted at reference ground tracks, RGTs), and up to 16 satellite passes per day over both the Arctic and the Southern Ocean. The along-track surface heights are generated by aggregating 150 geolocated signal photon heights from the primary science Level 2A ATL03 data product (Neumann et al., 2019). ATL10 data coverage is limited to areas that have an ice concentration > 50% (15% for ATL07), as inferred from passive microwave satellite measurements, and up to 25 km distance from land. A full description of the ATL07/10 products can be found in the Algorithm Theoretical Basis Document (ATBD, Kwok et al., 2021a) and recent changes to the algorithm are further discussed in (Kwok et al., 2021b). In this study we use release 003 (r003) ATL10 data.

In ATL10, the SSHA represents the measured sea surface elevation relative to a multi-year mean sea surface (MSS, see Section 2.3) after various geophysical and atmospheric corrections have been applied (see Table S1). Note that we adjust the solid earth tide correction included in each ICESat-2 segment's SSHA from r003 ATL10 data to correct a discrepancy in the permanent tide system. The adjustment is described in the supporting information (Text S1).

The SSHA is provided for each beam at three different length-scales: (1) segments classified as sea surface after radiometric classification as specular returns and height filtering, where SSHA measurements are calculated by fitting impulse-response weighted Gaussians to the height distribution of 150 photons within a segment (~20 m mean along-track SSH segment resolution for the strong beams); (2) individual leads, where the SSHA is calculated as the weighted mean height from consecutive segments forming an individual lead; (3) ~10-km along-track sections, where SSHA is calculated as the weighted mean of all leads within a given section for each beam, or linearly interpolated from adjacent sections, and smoothed using a 3-point point smoother. In subsequent analyses we use (1) – *height_segmet_height*, where *ssh_flag* = 2– but note that ATL21 data products will be formed using (3) to be consistent with the reference sea surface heights used to calculate freeboards (ATL10 and ATL20). This choice does not introduce significant differences in the gridded SSHA estimates (not shown) but allows us to take advantage of higher spatial resolution and of non-interpolated data when comparing results with CryoSat-2.

2.2 CryoSat-2 data

We use data acquired by the SIRAL K_u band SAR altimeter in the SAR mode, one of CryoSat-2's three modes of operation. We use intermediate Level 2 (L2) ice products processed at Baseline-D (Meloni et al., 2020) and available from ESA's CryoSat-2 Science Server (https://science-pds.cryosat.esa.int/). L2 data provide geolocated height measurements above the reference ellipsoid (WGS84) computed from each echo at intervals of approximately 300 meters. The data are already corrected for instrument effects, propagation delays, measurement geometry, and other geophysical effects (e.g., atmospheric delays and tides, see Table S1). In Table S2 and Figure S1 we provide an assessment of the differences between the ICESat-2 and

CryoSat-2 geophysical corrections, estimated from orbit cross-overs (coincident data filtered using a maximum time difference of 10 minutes and spatial difference of 10 km). Waveform retracking is also already applied in L2 data and determined using a model-fitting method to specular lead waveforms described by Giles et al. (2007). Further details and information can be found in the CryoSat-2 Baseline D Product Handbook (ESA, 2019) and in Meloni et al. (2020). Data coverage is controlled by the operational geographical mode mask (https://earth.esa.int/web/guest/-/geographical-mode-mask-7107) and updated every two weeks to account for changes in sea-ice extent.

2.3 Mean sea surface (MSS)

To consistently compute the SSHA for CryoSat-2 we remove a mean sea surface height from each ellipsoidal elevation from L2 data (*height_sea_ice_lead_20_ku*, which includes all instrumental and geophysical corrections) by bilinearly interpolating MSS values from a 2.5 km grid (Kwok et al., 2020 – https://zenodo.org/record/4294048) to the interval centroids. The MSS grid and the interpolation approach are the same as those used in the ICESat-2 sea ice data products. The MSS includes the geoid component and is in the mean-tide system (see Text S1), and is derived from CryoSat-2 SSH retrievals during 2011-2015 (Kwok & Morison, 2016) with gaps filled mainly at lower latitudes using the DTU13 global high resolution MSS (data from 10 satellite missions from 1992-2012; Andersen et al., 2016).

2.4 SSHA data binning and gridding

In along-track comparisons for the *CRYO2ICE* campaign (Figure 1, Section 3.1), we first identify measurement overlaps by selecting ICESat-2 SSHA segments from a given beam that fall within the theoretical CryoSat-2 pulse-limited across-track footprint (±825 m across-track from the centroid of each footprint; Scagliola, 2013). We then bin individual SSHA segments for ICESat-2 and SSHA intervals for CryoSat-2 in coincident 10-km sections (following the ATL10 sea ice product and based on the average Rossby radius of deformation for polar latitudes Chelton et al., 1998) and calculate the simple mean value from all measurements within each bin (shown as stars in Figure 1). For each profile we calculate the mean (μ) and standard deviation (*SD*) of the differences from all bins, and the correlation coefficient (*R)* between the two datasets.

To generate composite maps of the Arctic Ocean SSHA, along-track data from ICESat-2 and CryoSat-2 are first reprojected from the WGS 84 (EPSG:4326) to the NSIDC Sea Ice Polar Stereographic North coordinate system (EPSG:3411). The SSHA data are then gridded to the 25-km SSM/I polar stereographic grid (as in ATL20 and the upcoming ATL21 data products) by calculating the mean value within each grid cell for all data acquired within a given time period. Finally, we apply to both datasets a mask based on the NSIDC Arctic regional mask, in order to limit our assessment to the Beaufort, Chukchi, East Siberian, Laptev, Kara, Barents, and Greenland seas, and the Central Arctic (see Figure S2 and black dashed outline in maps shown in Figure 2-4).

3 Results and discussion

3.1 Along-track CRYO2ICE SSHA comparison

There have been 77 orbit alignments between ICESat-2 and CryoSat-2 between the start of the *CRYO2ICE* campaign on 4 August 2020 (ICESat-2 RGT 606) and 11 November 2020 (ICESat-2 RGT 739), the date of the last available ICESat-2 r003 ATL10 dataset. For some of these alignments the data products are not available and for many others, SSH data are missing/invalid (e.g., because of cloud cover for ICESat-2). From the subset of available data (Figure S3), we find 4 overlaps that extend for at least 400 km with >1000 valid sea surface height segments/intervals.

Figure 1 shows the along-track SSHA estimates for the four selected *CRYO2ICE* overlaps (12 August to 22 September 2020). Of the four examples, three (14, 15 August and 22 September, Figure 1b-d) show mean differences of 0.01 m and one (12 August, Figure 1a) of –0.03 m. The standard deviations are 0.02–0.03 m and the correlation coefficients (R) vary between 0.83 and 0.90. The relative differences between 10-km SSHA sections are shown in Figure S4 together with differences between geophysical corrections (i.e., tides and inverted barometer). Note that applying the geophysical corrections is key when doing these comparisons, as the lack of time-coincidence can cause significant (up to 20 cm) differences (Figure S4).

The larger (> 0.20 m) SSHA excursion shown in both datasets (referenced to the same MSS) in Figure 1b and smaller but still significant short-scale variability in the other profiles may be localized geoid features (e.g., associated to deep ocean ridges) that are not represented properly in the current MSS, and unlikely to be ocean circulation features.

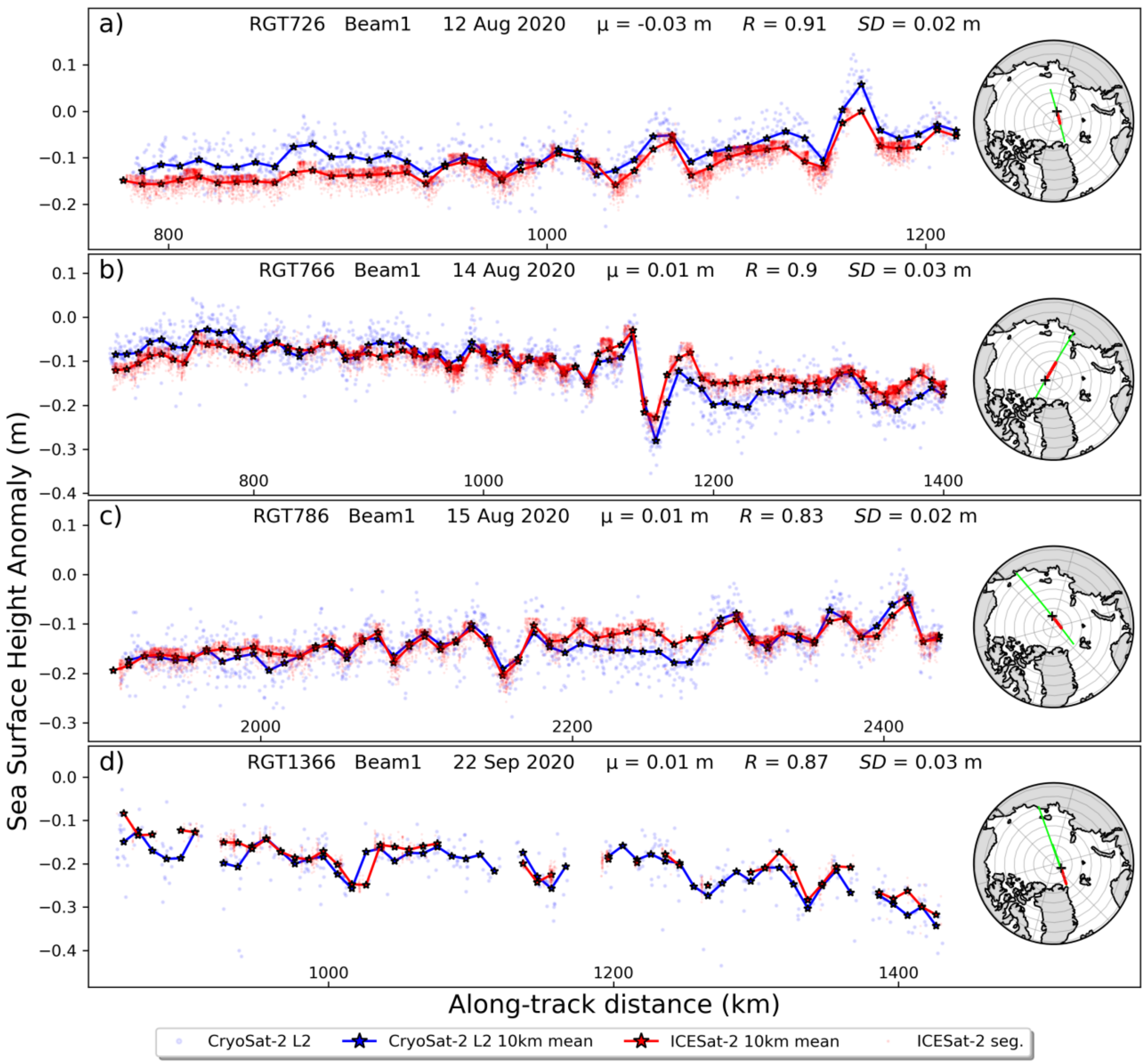

Figure 1: *CRYO2ICE* along-track SSHA comparisons. Red dots represent ICESat-2 sea surface segments, red stars show the mean value for 10-km sections. Blue dots represent CryoSat-2 sea surface intervals and blue stars the mean value for the same 10-km sections as for ICESat-2. The RGT number identifies the ICESat-2 reference ground track number. The date of acquisition of both datasets (separated by ~3 hours) is shown for each panel. For each overlap we report the mean difference (μ), the standard deviation (*SD*) of differences between the two datasets, and the correlation coefficient *R* from the least-squares regression. Map insets show the CryoSat-2 ground track in green and the extent of the overlap with the ICESat-2 beam footprint in red. The black + symbol marks the beginning of the profile (left side in main panels).

3.2 ICESat-2 beam comparison

Preliminary analyses by the ICESat-2 Project Science Office (PSO) have suggested that the ATLAS beams have different range biases and that these can vary through time – i.e. the height profiles from the 6 beams are not yet fully calibrated/reconciled and centimeter-level differences between beams remain. To understand the inter-beam range variability from SSHA estimates we calculate the monthly mean SSHA value over the Arctic since the start of the mission for the three strong beams independently (Figure 2a). The monthly SSHA estimate from beam 1 presents the largest differences with respect to the two other strong beams (up to ~ 0.07 m in July 2019) while differences between beam 3 and beam 5 are consistently ≤ 0.02 m. Correlation coefficients are 0.76, 0.66, and 0.93 for beam 1 – beam 3, beam 1 – beam 5, and beam 3 – beam 5, respectively. In Figure 2b-d we show the spatial distribution of the beam-to-beam differences for a given month (January 2019, gray bar in Figure 2a), which show that differences exhibit no obvious spatial correlation. This remains valid for all months since the start of the mission. The same beam-to-beam differences are also shown as histograms in Figure 2e-g, further demonstrating the clear inter-beam bias associated with beam 1 (mean of -0.03 m when compared to beam 3 and 5) and that differences between beam 3 and 5 are normally distributed around a mean of 0.00 m with a standard deviation of 0.05 m. The significant larger differences with beam 1 are also consistent with the findings of Brunt et al. (2021) estimated over the interior ice sheets of Antarctica (beam 1-3: 0.039 m; 1-5: 0.036 m; 3-5: 0.003 m), suggesting that these are sensor- or pointing solution-related.

For all of our subsequent analyses (Section 3.3 and 3.4), and until range differences between beams are fully characterized, we opt to use just a single strong beam when estimating Arctic SSHA. Based on the results presented above we select the middle strong beam (beam 3) since, despite its lower transmitted energy level (~80% of beam 1 and 5), the steeper incidence angle results in a stronger backscatter in the presence of highly reflective surfaces (e.g., leads) consistently increasing the number of specular lead returns compared to other strong beams (Kwok et al., 2021b). This is currently our recommended strategy for the initial production and release of ICESat-2 ATL21 data.

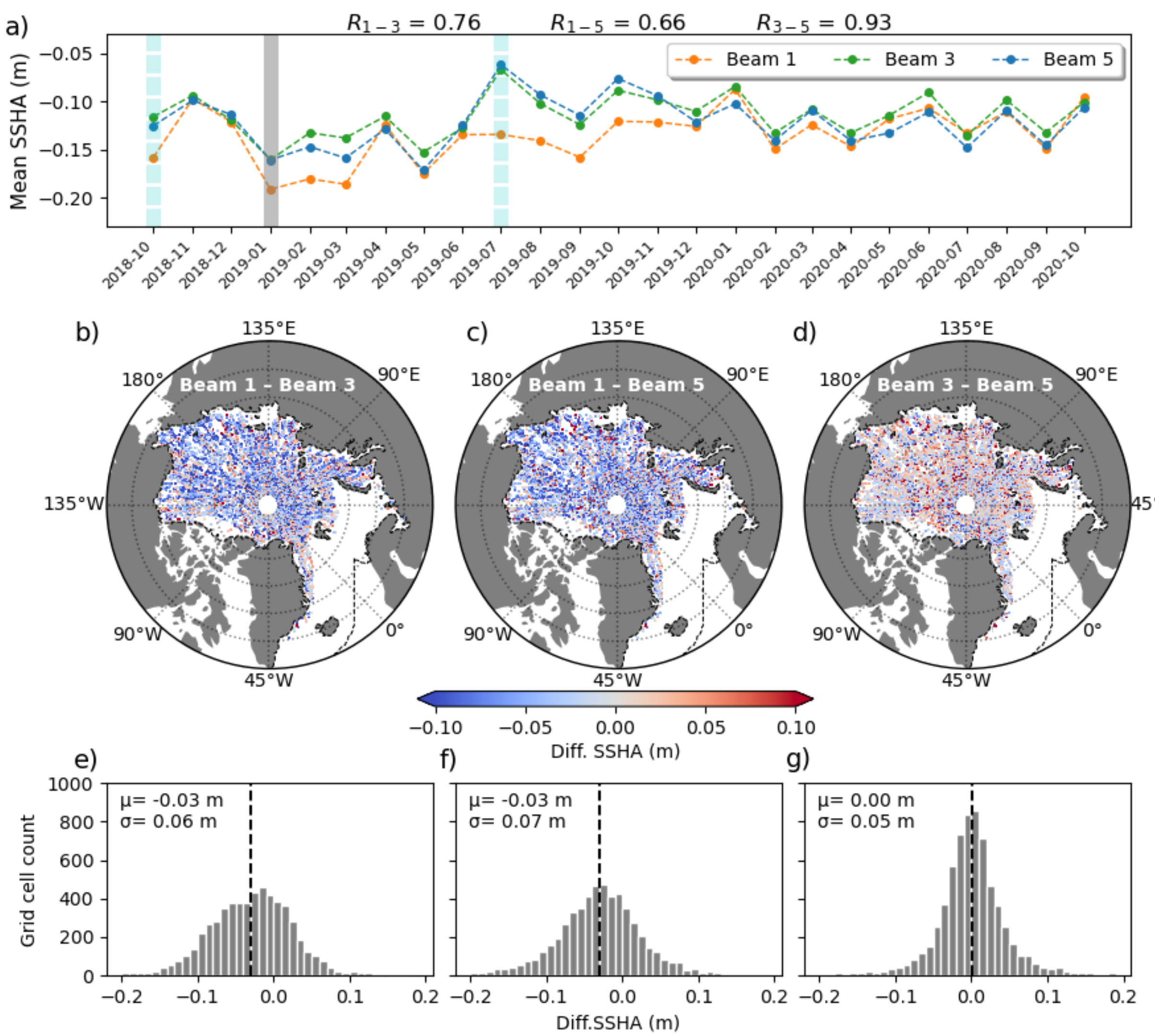

Figure 2: ICESat-2 beam comparison. **a)** Monthly mean for the Arctic Ocean calculated using data from each beam. The cyan dashed bars mark months for which data do not cover the entire month, October 2018–beginning of science data acquisition on 14 October– and July 2019–data between 1 and 8 July are not available due to satellite safe mode operations. The gray bar marks the month for which data are shown in panel b-g. Correlation coefficients (R) between beams are

shown at the top. **b-d)** Maps showing the differences between beams for the month of January 2019. The black dashed line marks the extent of the area of interest. **e-g)** histograms showing the distribution of the differences presented in panels b-d. The black dash lines mark the mean (μ) and σ is the standard deviation.

3.3 Monthly and multi-year SSHA comparison

In Figure 3a we compare monthly SSHA means calculated using ICESat-2 beam 3 to those calculated using CryoSat-2 L2 data. We limit this comparison to the Central Arctic, the area outlined by the green dashed line in Figure 3b (from NSIDC Arctic regional mask), where we expect consistent year-round ice cover and to exclude effects introduced by season-dependent changes in sea-ice extent and different data coverage near the coastal regions. Further details for each monthly comparison (mean, number of valid grid cells, number of data points) are provided in Table S3. Differences across all months between the two sensors have a mean of 0.01 m (SD = 0.02 m), and the correlation coefficient from a least-squares regression (*R)* is 0.76 (slope = 0.95, intercept = – 0.02 m). We find that up to 0.03 m of the observed monthly SSHA differences, especially during fall/winter, are caused by differences in the inverted barometer correction applied to each dataset (see also Table S2 and Figure S1). Our comparisons between heights from ICESat-2 with those from CryoSat-2 show a better agreement than has been shown by Brunt et al. (2021), who compared absolute ice height over the flat interiors of the Antarctic ice sheet and found differences > 0.3 m. This larger discrepancy, however, is likely due to the much greater penetration depth of the K_u band radar in firn compared to sea water.

We then compare the Arctic SSHA calculated from data spanning the two-year mission overlap, from 1 November 2018 through 31 October 2020. The ICESat-2 mean 2018-2020 SSHA in shown in Figure 3b and that from CryoSat-2 is presented in Figure 3c. Both maps show a positive SSHA in the southern Beaufort Sea, a strong negative anomaly in the

Chukchi/Siberian seas and a weaker negative SSHA in Central Western Arctic, a spatial pattern consistent with recent positive phase in the Arctic Oscillation (Armitage et al., 2018; Morison et al., 2021). In Figure 3d we show a histogram of the differences between ICESat-2 and CryoSat-2 SSHA, while a map of the SSHA differences is presented in Figure 3e, which shows the ICESat-2 SSHA to be generally higher in the more marginal seas (Barents, Kara, East Siberian, and Chukchi) and slightly lower in the Central Arctic. The marginal seas are areas of large SSH variability where the different acquisition times between the two satellites can capture different parts of these cycles (see Figure S5 for the standard deviation of each dataset, showing higher values in the marginal seas) and can therefore explain much of these differences. Increased data acquisition from both missions will enable a more reliable comparison of the mean SSHA from ICESat-2 and CryoSat-2.

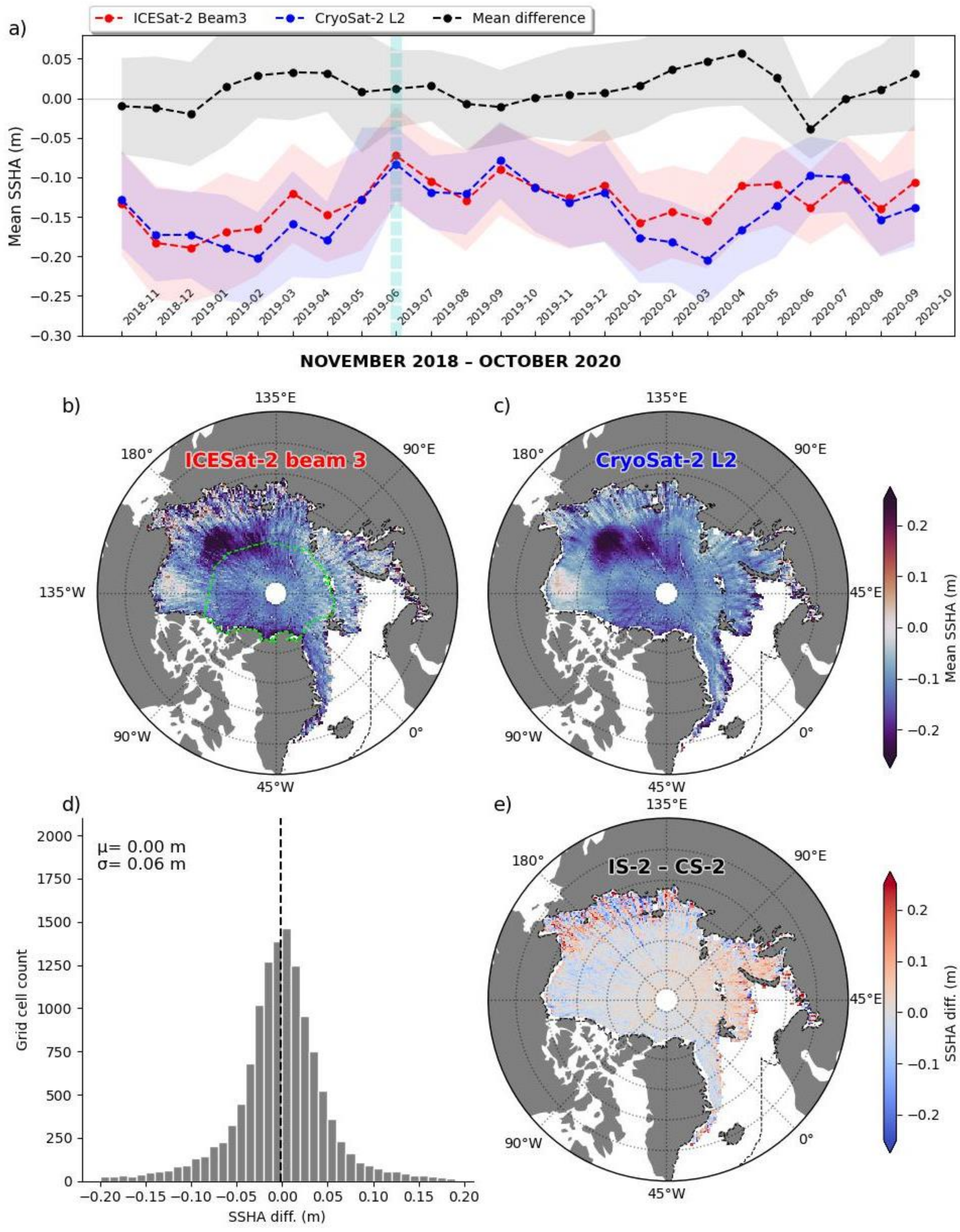

Figure 3: Comparison between ICESat-2 and CryoSat-2 Arctic SSHA. **a)** time series of monthly mean SSHA for the Central Arctic (area outlined by green dashed-line in panel b) from ICESat-2 (red) and CryoSat-2 (blue), with shaded areas representing one standard deviation from the

mean. **b-c)** Multi-year mean SSHA estimated using data acquired between 1 November 2018 and 31 October 2020. **d)** Histogram showing the distribution of the differences between ICESat-2 and CryoSat-2, also shown in map view in panel **e)**. In d) the black dash line marks the mean (μ) and σ is the standard deviation. The black dashed line in e) marks the extent of the area of interest (data outside this line are masked out).

3.4 Seasonal SSHA variations from ICESat-2

In Figure 4 we present seasonal maps of Arctic SSHA for three-month periods starting in mid-October 2018 and ending in September 2020. The top row (Figure 4a-d) can be directly compared to the bottom row (Figure 4e-h) to assess year-to-year differences, while from left to right we track the temporal progression during two entire freezing-melting seasons (2018–2019 and 2019–2020). Note that variations in spatial coverage are dictated by variations in sea ice extent since ICESat-2 ATL10 data are only provided for areas that have an ice concentration > 50%. Comparisons to CryoSat-2 for each three-month period are presented in Figure S6, and confirm similar SSHA spatio-temporal variations providing some confidence in the capability of ICESat-2 to produce consistent estimates of Arctic SSHA.

A positive SSHA centered on the Beaufort Sea (a strengthened Beaufort Gyre) is clearly visible during winter months but less apparent in 2020 (see Figure 4 c-d compared to Figure 4 g-h). Large variability in the Siberian and Chukchi seas also corresponds to areas characterized by high short-term SSH variability.

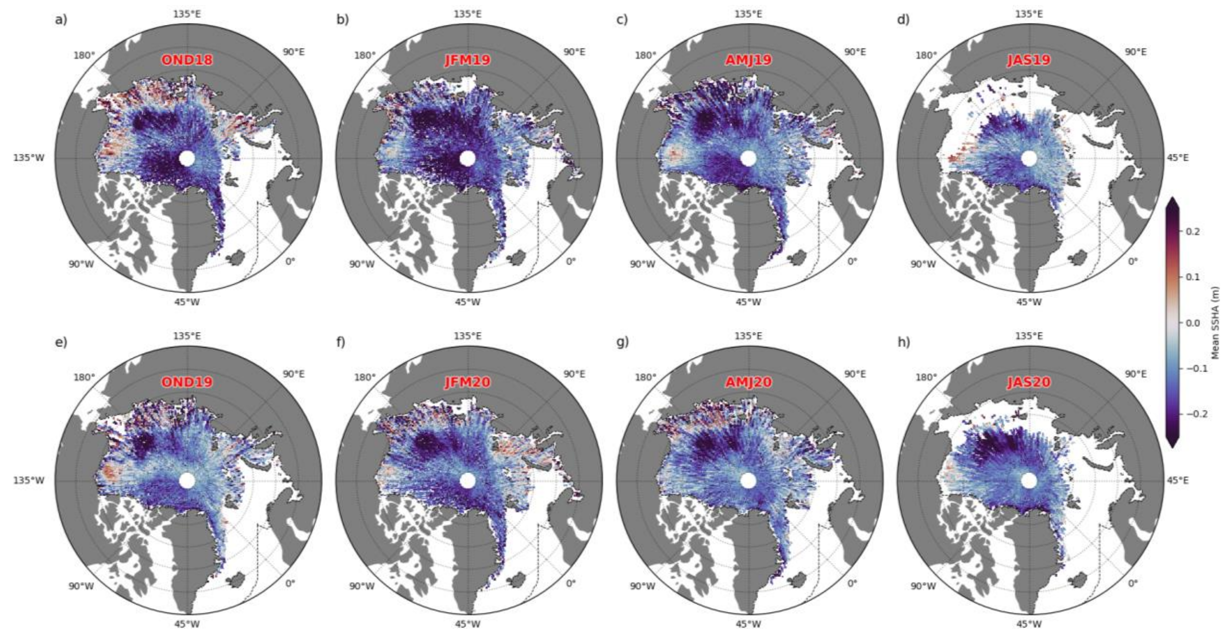

Figure 4: Seasonal mean SSHA maps from ICESat-2. OND = October, November, December; JFM = January, February, March; AMJ = April, May, June; JAS = July, August, September. The black dashed line marks the extent of the area of interest (data outside this line are masked out).

5 Summary and conclusions

Here we have presented a first examination of Arctic sea surface height anomalies (SSHA) from NASA's ICESat-2 laser altimeter during the first two years of the mission (2018-2020). We analyzed beam-to-beam differences and provided an independent assessment of inter-beam range biases for the ATLAS altimeter. We compared the ICESat-2 SSHA estimates with L2 sea ice data obtained from ESA's CryoSat-2 radar altimeter. We provided a brief description of the necessary steps to compare the SSHA data from the two altimetry missions by imposing the same permanent tide system and MSS. A careful reconciliation of the data (e.g., same geophysical corrections) is needed in future efforts to blend data from ICESat-2 with those from CryoSat-2 (and potentially other airborne and space-borne altimetry missions).

The strong agreement between both the semi-synchronous along-track estimates from the *CRYO2ICE* overlaps and basin-scale gridded SSHA estimates between the two sensors suggests that the higher resolution ICESat-2 data can be used to estimate monthly/seasonal SSHA and perhaps resolve 10 km-scale spatial variability in SSHA. The multi-year record of overlap also opens up the potential to produce a new, high-resolution, blended, estimate of the mean sea surface of the Arctic Ocean (and indeed Southern Ocean) which could rectify what we believe to be unphysically large short-scale variations in SSHA shown in the *CRYO2ICE* overlaps. Finally, our results provide a first evaluation of the approach used for the production of ICESat-2 SSHA gridded data products for the polar oceans (ATL21). Future work will extend this analysis to the Southern Ocean, pending *CRYO2ICE* orbit maneuvers for the Southern Hemisphere.

Acknowledgments

The authors would like to thank the entire ICESat-2 project for their continued efforts in delivering and maintaining the high-quality sea ice data analyzed in this study. The manuscript greatly benefited from the comments of two anonymous reviewers and from discussions with Rachel Tilling, Steven Fons and other sea ice and oceanography members of the ICESat-2 team.

Data Availability Statement

ICESat-2 ATL10 data products (freeboard) were obtained from NSIDC and are available at http://nsidc.org/data/atl10. CryoSat-2 Level-2 data (SIR_SAR_L2) were obtained from ESA at https://science-pds.cryosat.esa.int/#. The mean sea surface grid is available at https://zenodo.org/record/4294048. Monthly gridded SSHA estimates for the Arctic Ocean derived in this study are available on Zenodo: https://doi.org/10.5281/zenodo.4707371

References

Andersen, O., Knudsen, P., & Stenseng, L. (2016). The DTU13 MSS (Mean Sea Surface) and MDT (Mean Dynamic Topography) from 20 Years of Satellite Altimetry. In S. Jin & R. Barzaghi (Eds.), *IGFS 2014* (pp. 111–121). Springer International Publishing.

Armitage, T. W. K., Bacon, S., & Kwok, R. (2018). Arctic Sea Level and Surface Circulation Response to the Arctic Oscillation. *Geophysical Research Letters*, *45*(13), 6576–6584. https://doi.org/10.1029/2018GL078386

Armitage, T. W. K., Bacon, S., Ridout, A. L., Thomas, S. F., Aksenov, Y., & Wingham, D. J. (2016). Arctic sea surface height variability and change from satellite radar altimetry and GRACE, 2003-2014. *Journal of Geophysical Research: Oceans*, *121*(6), 4303–4322. https://doi.org/10.1002/2015JC011579

Armitage, T. W. K., & Davidson, M. W. J. (2014). Using the Interferometric Capabilities of the ESA CryoSat-2 Mission to Improve the Accuracy of Sea Ice Freeboard Retrievals. *IEEE Transactions on Geoscience and Remote Sensing*, *52*(1), 529–536. https://doi.org/10.1109/TGRS.2013.2242082

Armitage, T. W. K., Manucharyan, G. E., Petty, A. A., Kwok, R., & Thompson, A. F. (2020). Enhanced eddy activity in the Beaufort Gyre in response to sea ice loss. *Nature Communications*, *11*(1), 761. https://doi.org/10.1038/s41467-020-14449-z

Brunt, K. M., Smith, B. E., Sutterley, T. C., Kurtz, N. T., & Neumann, T. A. (2021). Comparisons of Satellite and Airborne Altimetry With Ground-Based Data From the Interior of the Antarctic Ice Sheet. *Geophysical Research Letters*, *48*(2). https://doi.org/10.1029/2020GL090572

Chelton, D. B., Deszoeke, R. A., Schlax, M. G., Naggar, K. E., & Siwertz, N. (1998). Geographical Variability of the First Baroclinic Rossby Radius of Deformation. *JOURNAL OF PHYSICAL OCEANOGRAPHY*, *28*, 28.

Di Bella, A., Kwok, R., Skourup, H., & Forsberg, R. (2020). Multi-peak Retracking of CryoSat-2 SARIn Waveforms Over Arctic Sea Ice. *IEEE TRANSACTIONS ON GEOSCIENCE AND REMOTE SENSING*, 17.

Giles, K.A., Laxon, S. W., Wingham, D. J., Wallis, D. W., Krabill, W. B., Leuschen, C. J., McAdoo, D., Manizade, S. S., & Raney, R. K. (2007). Combined airborne laser and radar altimeter measurements over the Fram Strait in May 2002. *Remote Sensing of Environment*, *111*(2–3), 182–194. https://doi.org/10.1016/j.rse.2007.02.037

Giles, Katharine A., Laxon, S. W., Ridout, A. L., Wingham, D. J., & Bacon, S. (2012). Western Arctic Ocean freshwater storage increased by wind-driven spin-up of the Beaufort Gyre. *Nature Geoscience*, *5*(3), 194–197. https://doi.org/10.1038/ngeo1379

Kwok, R., Kacimi, S., Markus, T., Kurtz, N. T., Studinger, M., Sonntag, J. G., Manizade, S. S., Boisvert, L. N., & Harbeck, J. P. (2019). ICESat-2 Surface Height and Sea Ice Freeboard Assessed With ATM Lidar Acquisitions From Operation IceBridge. *Geophysical Research Letters*, *46*(20), 11228–11236. https://doi.org/10.1029/2019GL084976

Kwok, R., & Morison, J. (2011). Dynamic topography of the ice-covered Arctic Ocean from ICESat. *Geophysical Research Letters*, *38*(2), n/a-n/a. https://doi.org/10.1029/2010GL046063

Kwok, Ron, Petty, A., Cunningham, G. F., Hancock, D. W., Ivanoff, A., Wimert, J. T., Bagnardi, M., & Kurtz, N. (2021a). *Algorithm Theoretical Basis Document (ATBD) For Sea Ice Products. https://nsidc.org/sites/nsidc.org/files/technical-references/ICESat2_ATL07_ATL10_ATL20_ATL21_ATBD_r004.pdf*

Kwok, R., Petty, A. A., Bagnardi, M., Kurtz, N. T., Cunningham, G. F., Ivanoff, A., & Kacimi, S. (2021b). Refining the sea surface identification approach for determining freeboards in the ICESat-2 sea ice products. *The Cryosphere*, *15*(2), 821–833. https://doi.org/10.5194/tc-15-821-2021

Kwok, Ron, & Morison, J. (2016). Sea surface height and dynamic topography of the ice-covered oceans from CryoSat-2: 2011–2014. *Journal of Geophysical Research: Oceans*, *121*(1), 674–692. https://doi.org/10.1002/2015JC011357

Magruder, L. A., Brunt, K. M., & Alonzo, M. (2020). Early ICESat-2 on-orbit Geolocation Validation Using Ground-Based Corner Cube Retro-Reflectors. *Remote Sensing*, *12*(21), 3653. https://doi.org/10.3390/rs12213653

Meloni, M., Bouffard, J., Parrinello, T., Dawson, G., Garnier, F., Helm, V., Di Bella, A., Hendricks, S., Ricker, R., Webb, E., Wright, B., Nielsen, K., Lee, S., Passaro, M., Scagliola, M., Simonsen, S. B., Sandberg Sørensen, L., Brockley, D., Baker, S., … Mizzi, L. (2020). CryoSat Ice Baseline-D validation and evolutions. *The Cryosphere*, *14*(6), 1889–1907. https://doi.org/10.5194/tc-14-1889-2020

Morison, J., Kwok, R., Dickinson, S., Andersen, R., Peralta-Ferriz, C., Morison, D., Rigor, I., Dewey, S., & Guthrie, J. (2021). The Cyclonic Mode of Arctic Ocean Circulation. *Journal of Physical Oceanography*. https://doi.org/10.1175/JPO-D-20-0190.1

Morison, J., Kwok, R., Peralta-Ferriz, C., Alkire, M., Rigor, I., Andersen, R., & Steele, M. (2012). Changing Arctic Ocean freshwater pathways. *Nature*, *481*(7379), 66–70. https://doi.org/10.1038/nature10705

Neumann, T. A., Martino, A. J., Markus, T., Bae, S., Bock, M. R., Brenner, A. C., Brunt, K. M., Cavanaugh, J., Fernandes, S. T., Hancock, D. W., Harbeck, K., Lee, J., Kurtz, N. T., Luers, P. J., Luthcke, S. B., Magruder, L., Pennington, T. A., Ramos-Izquierdo, L., Rebold, T., … Thomas, T. C. (2019). The Ice, Cloud, and Land Elevation Satellite – 2 mission: A global geolocated photon product derived from the Advanced Topographic Laser Altimeter System. *Remote Sensing of Environment*, *233*, 111325. https://doi.org/10.1016/j.rse.2019.111325

Parrinello, T., Shepherd, A., Bouffard, J., Badessi, S., Casal, T., Davidson, M., Fornari, M., Maestroni, E., & Scagliola, M. (2018). CryoSat: ESA's ice mission – Eight years in space. *Advances in Space Research*, *62*(6), 1178–1190. https://doi.org/10.1016/j.asr.2018.04.014

Peacock, N. R., & Laxon, S. W. (2004). Sea surface height determination in the Arctic Ocean from ERS altimetry. *J. Geoph. Res.*, 109, C0700. https://doi.org/10.1029/2001JC001026

Petty, A. A., Bagnardi, M., Kurtz, N., Tilling, R., Fons, S., Armitage, T., Horvat, C., & Kwok, R. (2021). Assessment of ICESat-2 sea ice surface classification with Sentinel-2 imagery: Implications for freeboard and new estimates of lead and floe geometry. *Earth and Space Science*, *8*, e2020EA001491. https://doi.org/10.1029/2020EA001491

Polyakov, I. V., Pnyushkov, A. V., Alkire, M. B., Ashik, I. M., Baumann, T. M., Carmack, E. C., Goszczko, I., Guthrie, J., Ivanov, V. V., Kanzow, T., Krishfield, R., Kwok, R., Sundfjord, A., Morison, J., Rember, R., & Yulin, A. (2017). Greater role for Atlantic inflows on sea-ice loss in the Eurasian Basin of the Arctic Ocean. *Science, 356*(6335), 285–291. https://doi.org/10.1126/science.aai8204

Proshutinsky, A., Krishfield, R., Toole, J. M., Timmermans, M. -L., Williams, W., Zimmermann, S., Yamamoto-Kawai, M., Armitage, T. W. K., Dukhovskoy, D., Golubeva, E., Manucharyan, G. E., Platov, G., Watanabe, E., Kikuchi, T., Nishino, S., Itoh, M., Kang, S. -H., Cho, K. -H., Tateyama, K., & Zhao, J. (2019). Analysis of the Beaufort Gyre Freshwater Content in 2003–2018. *Journal of Geophysical Research: Oceans*, *124*(12), 9658–9689. https://doi.org/10.1029/2019JC015281

Scagliola, M. (2013). *CryoSat footprints–Aresys Technical Note*. SAR-CRY2-TEN-6331, Aresys/ESA, Italy.

Timmermans, M., & Marshall, J. (2020). Understanding Arctic Ocean Circulation: A Review of Ocean Dynamics in a Changing Climate. *Journal of Geophysical Research: Oceans*, *125*(4). https://doi.org/10.1029/2018JC014378

Wingham, D. J., Francis, C. R., Baker, S., Bouzinac, C., Brockley, D., Cullen, R., de Chateau-Thierry, P., Laxon, S. W., Mallow, U., Mavrocordatos, C., Phalippou, L., Ratier, G., Rey, L., Rostan, F., Viau, P., & Wallis, D. W. (2006). CryoSat: A mission to determine the fluctuations in Earth's land and marine ice fields. *Advances in Space Research*, *37*(4), 841–871. https://doi.org/10.1016/j.asr.2005.07.027

Zwally, H. J., Schutz, B., Abdalati, W., Abshire, J., Bentley, C., Brenner, A., Bufton, J., Dezio, J., Hancock, D., Harding, D., Herring, T., Minster, B., Quinn, K., Palm, S., Spinhirne, J., & Thomas, R. (2002). ICESat's laser measurements of polar ice, atmosphere, ocean, and land. *Journal of Geodynamics*, *34*(3–4), 405–445. https://doi.org/10.1016/S0264-3707(02)00042-X

IPCC. *IPCC Special Report on the Ocean and Cryosphere in a Changing Climate* (IPCC, 2019). https://www.ipcc.ch/srocc/

Figure 1.

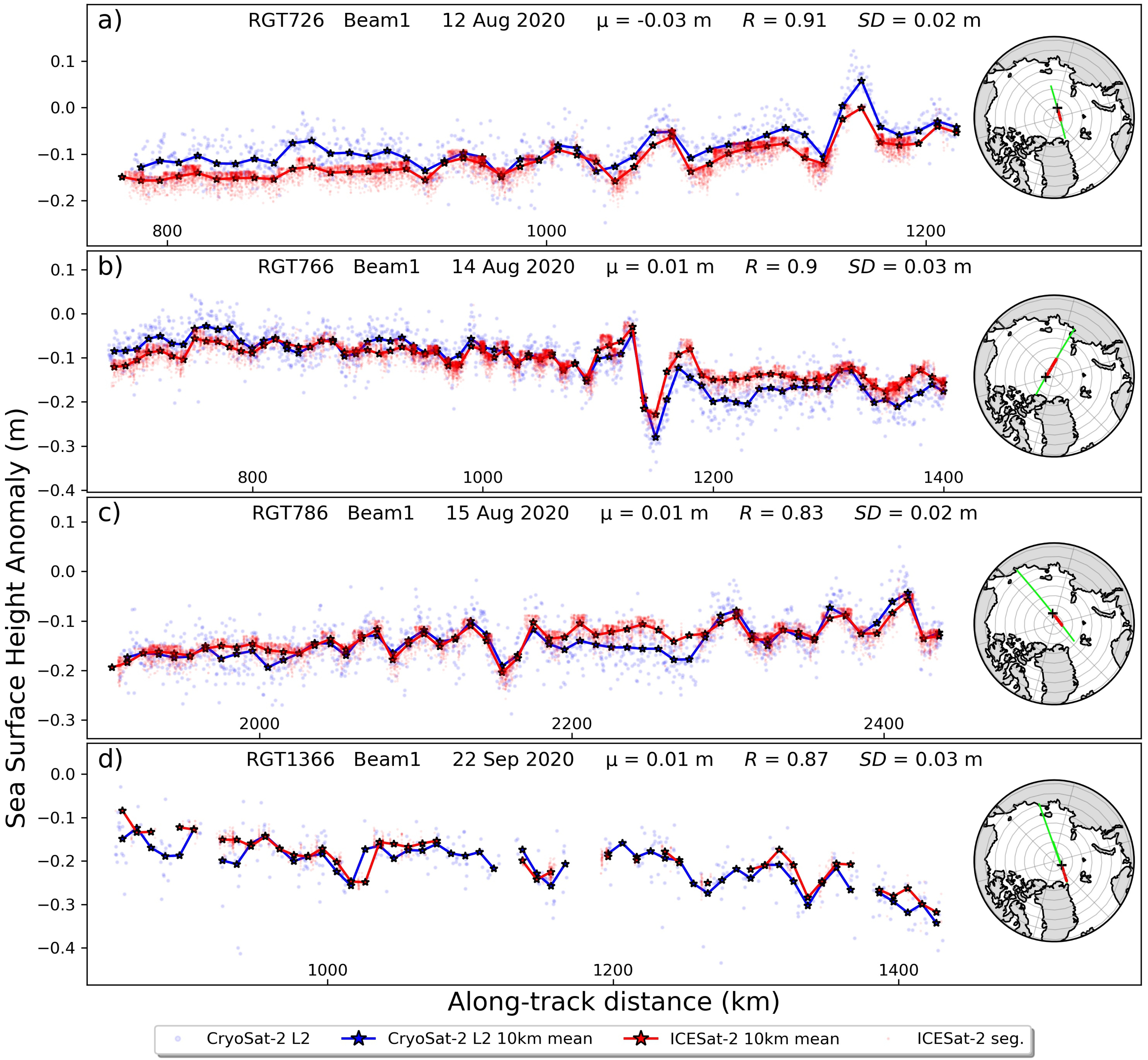

a) RGT726 Beam1 12 Aug 2020 μ = -0.03 m R = 0.91 SD = 0.02 m
b) RGT766 Beam1 14 Aug 2020 μ = 0.01 m R = 0.9 SD = 0.03 m
c) RGT786 Beam1 15 Aug 2020 μ = 0.01 m R = 0.83 SD = 0.02 m
d) RGT1366 Beam1 22 Sep 2020 μ = 0.01 m R = 0.87 SD = 0.03 m
Sea Surface Height Anomaly (m)
Along-track distance (km)
CryoSat-2 L2
CryoSat-2 L2 10km mean
ICESat-2 10km mean
ICESat-2 seg.

Figure 2.

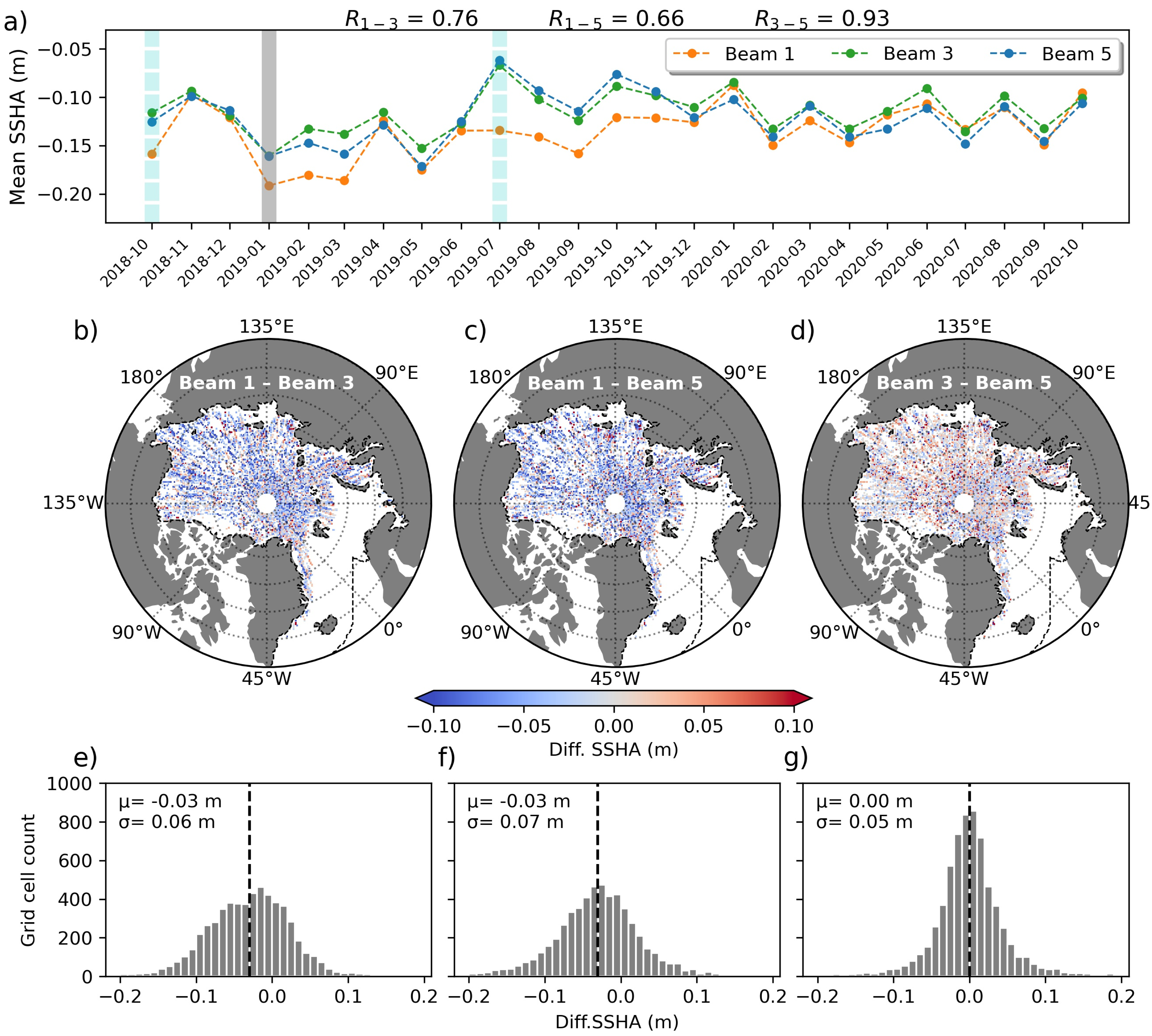
a)
R_{1-3} = 0.76
R_{1-5} = 0.66
R_{3-5} = 0.93
Beam 1
Beam 3
Beam 5
Mean SSHA (m)
−0.05
−0.10
−0.15
−0.20
2018-10
2018-11
2018-12
2019-01
2019-02
2019-03
2019-04
2019-05
2019-06
2019-07
2019-08
2019-09
2019-10
2019-11
2019-12
2020-01
2020-02
2020-03
2020-04
2020-05
2020-06
2020-07
2020-08
2020-09
2020-10
b)
c)
d)
Beam 1 – Beam 3
Beam 1 – Beam 5
Beam 3 – Beam 5
135°E
180°
90°E
135°W
45°E
90°W
0°
45°W
−0.10
−0.05
0.00
0.05
0.10
Diff. SSHA (m)
e)
f)
g)
μ= -0.03 m
σ= 0.06 m
μ= -0.03 m
σ= 0.07 m
μ= 0.00 m
σ= 0.05 m
Grid cell count
1000
800
600
400
200
0
−0.2
−0.1
0.0
0.1
0.2
Diff.SSHA (m)

Figure 3.

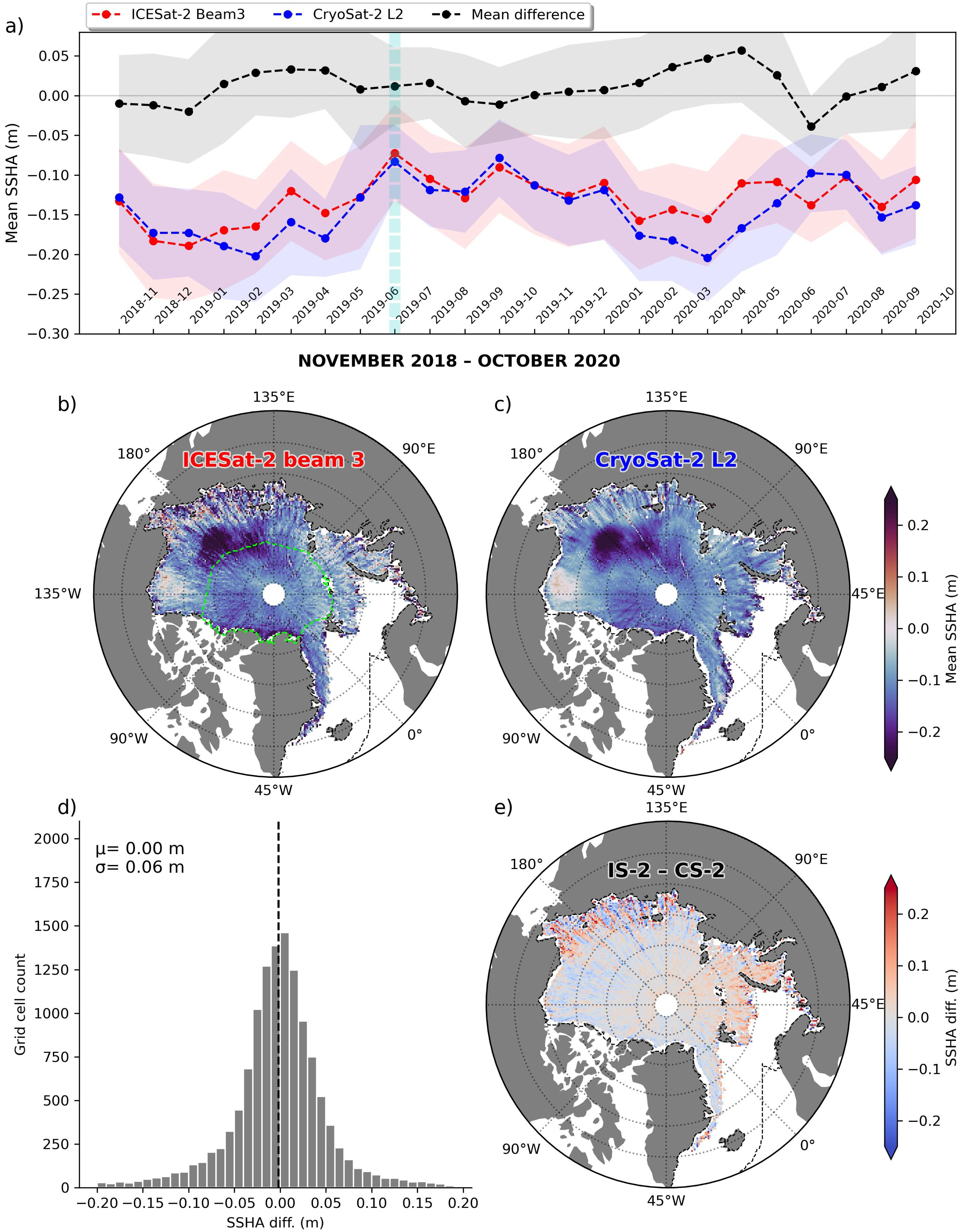

a)
ICESat-2 Beam3
CryoSat-2 L2
Mean difference
Mean SSHA (m)
NOVEMBER 2018 – OCTOBER 2020
b)
ICESat-2 beam 3
c)
CryoSat-2 L2
Mean SSHA (m)
d)
μ= 0.00 m
σ= 0.06 m
Grid cell count
SSHA diff. (m)
e)
IS-2 – CS-2
SSHA diff. (m)

Figure 4.

a)
OND18
b)
JFM19
c)
AMJ19
d)
JAS19
e)
OND19
f)
JFM20
g)
AMJ20
h)
JAS20
135°E
90°E
180°
135°W
45°E
90°W
0°
45°W
Mean SSHA (m)
0.2
0.1
0.0
−0.1
−0.2